



Analytical formulae for design of one-dimensional sonic crystals with smooth geometry based on symbolic regression

Viktor Hruška^{*}, Aneta Furmanová, Michal Bednařík

Faculty of Electrical Engineering, Czech Technical University in Prague, Technická 2, Prague, 166 27, Czech Republic

ARTICLE INFO

Keywords:

Sonic crystals
Symbolic regression
Physics-informed machine learning
Locally periodic structures

ABSTRACT

Even though locally periodic structures have been studied for more than three decades, the known analytical expressions relating the waveguide geometry and the acoustic transmission are limited to a few special cases. Having an access to numerical model is a great opportunity for data-driven discovery. Our choice of cubic splines to parametrize the waveguide unit cell geometry offers enough variability for waveguide design. Using Webster equation for unit cell and Floquet–Bloch theory for periodic structures, a dataset of numerical solutions was prepared. Employing the methods of physics-informed machine learning, we have extracted analytical formulae relating the waveguide geometry and the corresponding dispersion relation or directly the bandgap widths. The results contribute to the overall readability of the system and enable a deeper understanding of the underlying principles. Specifically, it allows for assessing the influence of the waveguide geometry, offering more efficient alternative to computationally demanding numerical optimization.

1. Introduction

Sonic (or phononic) crystals are macroscopic artificial periodic structures that can effectively modify the transmission of acoustic or elastic waves due to fluid–structure interactions or change of material properties in solids. Introduced more than three decades ago, they have attracted interest due to their remarkable transmission characteristics that are not achieved by any natural medium [1]. Therefore, they are often included in the broader field of acoustic metamaterials (see e.g., [2,3]). Since its beginnings the topic of sonic crystals has earned considerable attention and a captivating publication history that is now well summarized in a number of recent reviews [4,5]. In recent years, the spectrum of methods used has expanded to include some machine learning influences [6,7], and this paper follows this path.

Although there is a wide variety of analytical approaches and numerical methods to solve sonic crystal problems [8,9], analytical formulae to solve the bandgap parameters are known only for a few very special cases, such as the simplest chains (see e.g., [9,10]). However, interesting advances in this field have recently been made into the weakly nonlinear regime [11–13], yet only in discrete systems.

Naturally, there are many analogous scenarios from related fields of physics, such as photonics [14–17]. Here, however, we concentrate mainly on acoustic waves and some extensions for elastodynamics. Recently, Deng et al. [18] showed an interesting case of quasi 1D sonic crystal composed of unit cells with impedance walls resembling the sonic black hole configuration. Computationally it relies on a weak formulation of the equations and a use has been made of Gaussian basis functions [18,19].

To overcome the lack of analytical expressions for bandgaps in one-dimensional continuous geometries we utilize methods of data-driven science and physics-informed machine learning [20–24]. Similarly to Gupta et al. [25] or Deng et al. [18] we employ the

^{*} Corresponding author.

E-mail address: viktor.hruska@fel.cvut.cz (V. Hruška).

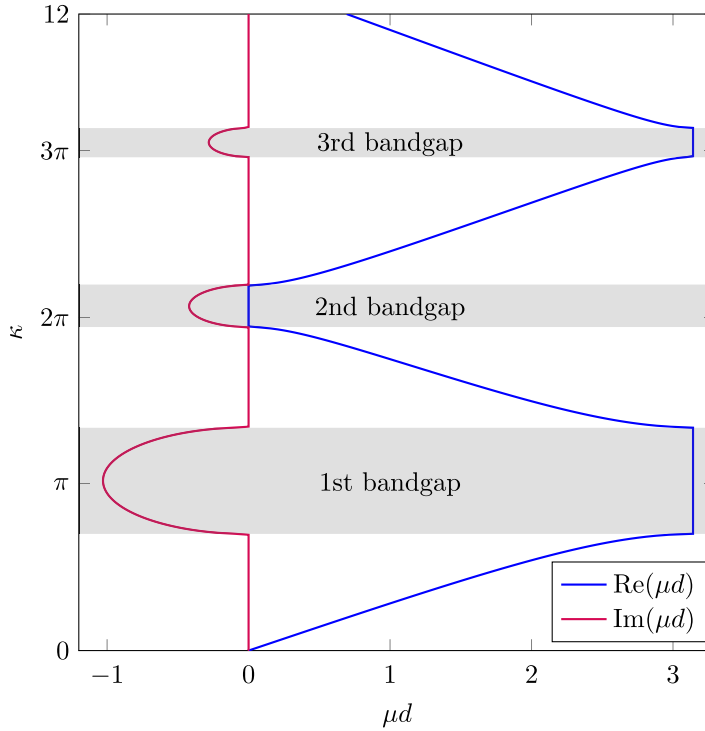


Fig. 1. Dispersion relation for geometry shown in Fig. 2. Details regarding the nondimensional variables are given in Section 2.

Webster equation to study the one-dimensional sonic crystal supporting quasi-plane wave propagation. Utilizing the Floquet–Bloch theory on a single unit cell (see e.g., [14–16]) we obtain the most distinctive representation of the wave transmission through a periodic structure: the dispersion relation showing the bandgaps (see Fig. 1). Subsequently, a large set of one-dimensional geometries is used to learn the descriptive equations.

The paper is organized as follows. In Section 2, the governing equation is introduced along with necessary elements of theory of wave propagation in periodic structures. Strategy for discovering analytical model from the data is outlined in Section 3. In Section 4, the retrieved formulae for acoustic transmission model and their practical applications are presented. Further possible applications of the results are discussed in Section 5, together with the effect of neglecting the thermoviscous losses on the transmission characteristics. Finally, the conclusions are drawn in Section 6.

2. Governing equation and implications of periodicity

In this section we show the application of the theory of sound propagation in locally periodic structures to the case of quasi-planar acoustic waves in a waveguide of a circular cross-section with non-uniform radius. Please note that due to the mathematical isomorphism this approach is the same for some other wave equations (see the Discussion in Section 5). We are using this particular case only for definiteness.

2.1. The Webster equation

In an acoustic waveguide of variable cross-section with perfectly rigid walls, the Webster wave equation (see e.g., [26]) holds for the propagation of quasi-plane waves:

$$\frac{\partial^2 p}{\partial s^2} + \frac{1}{A(s)} \frac{dA(s)}{ds} \frac{\partial p}{\partial s} = \frac{1}{c_0^2} \frac{\partial^2 p}{\partial t^2}, \quad (1)$$

where $p = p(s, t)$ is the acoustic pressure and s , t and $A = A(s)$ denote the spatial coordinate along the waveguide axis, time and cross-sectional area function, respectively (see Fig. 2). The adiabatic sound speed c_0 is given by $c_0^2 = \gamma p_0 / \rho_0$, with γ , p_0 and ρ_0 denoting the ratio of specific heats, ambient pressure and density, respectively. For simplicity, we choose a circular cross-section of the waveguide (some other options are given in the Discussion). Hence, $A(s) = \pi R(s)^2$.

Assuming the time-harmonic behavior (with the sign convention $e^{-i\omega t}$), the Eq. (1) can be expressed in the form

$$\frac{d^2 p}{ds^2} + \frac{2}{R} \frac{dR}{ds} \frac{dp}{ds} + \frac{\omega^2}{c_0^2} p = 0. \quad (2)$$

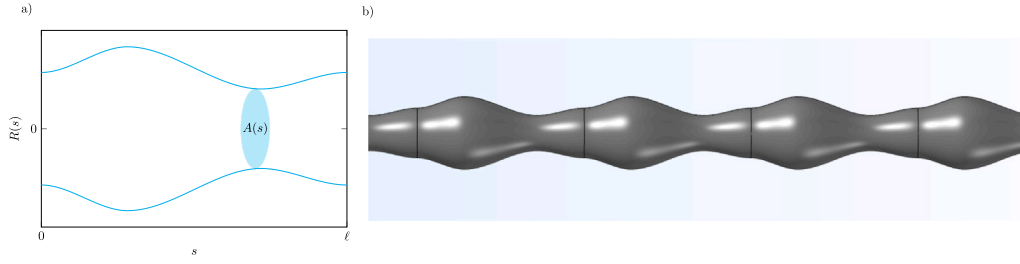


Fig. 2. (a) Waveguide of a circular cross-section with non-uniform radius function $R(s)$ and cross-sectional area function $A(s)$; (b) corresponding 3D render from COMSOL Multiphysics.

Introducing an axial characteristic length ℓ and a lateral characteristic length R_0 , the Webster equation (2) can be put in a non-dimensional form

$$\frac{d^2 \tilde{p}}{dx^2} + \frac{2}{r} \frac{dr}{dx} \frac{d\tilde{p}}{dx} + \kappa^2 \tilde{p} = 0, \quad (3)$$

where $x = s/\ell$, $r = R/R_0$, $\tilde{p} = p/\rho_0 c_0^2$ and $\kappa = \omega\ell/c_0$ denote the non-dimensional axial coordinate, local radius, acoustic pressure and wavenumber, respectively.

2.2. Elements of the Floquet–Bloch theory

Now, we assume that the radius function $r(x)$ is periodic with a period d so that $r(x) = r(x + d)$. Then the Floquet–Bloch theory suggests that

$$\tilde{p}(x + d) = \rho_{1,2} \tilde{p}(x), \quad (4)$$

so the problem of wave propagation in an infinite periodic structure can be recast into finding the multipliers $\rho_{1,2}$. Let $u(x)$ and $v(x)$ denote linearly independent solutions of Eq. (3) satisfying the initial conditions:

$$u(0) = 1, \quad u'(0) = 0, \quad v(0) = 0, \quad v'(0) = 1, \quad (5)$$

then the characteristic equation for the multipliers reads

$$\rho^2 - [u(d) + v'(d)]\rho + 1 = 0. \quad (6)$$

It follows that $\rho_1 \rho_2 = 1$ and hence they can be written as

$$\rho_{1,2} = \exp(\pm i\mu d), \quad (7)$$

where μ stands for the Bloch wavenumber. Moreover, solution of Eq. (6) shows that

$$\rho_1 + \rho_2 = u(d) + v'(d) \quad (8)$$

and using the substitution in Eq. (6) we can write

$$u(d) + v'(d) = \exp(i\mu d) + \exp(-i\mu d) = 2 \cos \mu d. \quad (9)$$

Hence, we can obtain cosine of the Bloch phase $\xi \equiv \mu d$ and the Bloch wave number μ as

$$\cos \xi = \frac{u(d) + v'(d)}{2}, \quad (10)$$

$$\mu = \frac{1}{d} \arccos \frac{u(d) + v'(d)}{2}. \quad (11)$$

Although the latter equations are indeed equivalent, we explicitly state both of them for the sake of the sections below.

Generally, the Bloch wave number is a function of the frequency of a quasi-plane wave propagating through a periodic structure and can take complex values ($\mu = \mu(\omega) \in \mathbb{C}$). It follows from Eqs. (4) and (7) that when the imaginary part of μ is non-zero, the propagation of the quasi-plane wave in the infinite periodic structure is not possible. Or, similarly, only evanescent waves are propagating through the locally periodic structure.

We study the system as a purely reactive one, without any dissipation (see the justification in Section 5.2). It follows that some phenomena related to the occurrence of significant losses would not take place, such as branch overtaking and cut-off studied by Hussein and Frazier [27] in the case of elastic waves in binary sonic crystals.

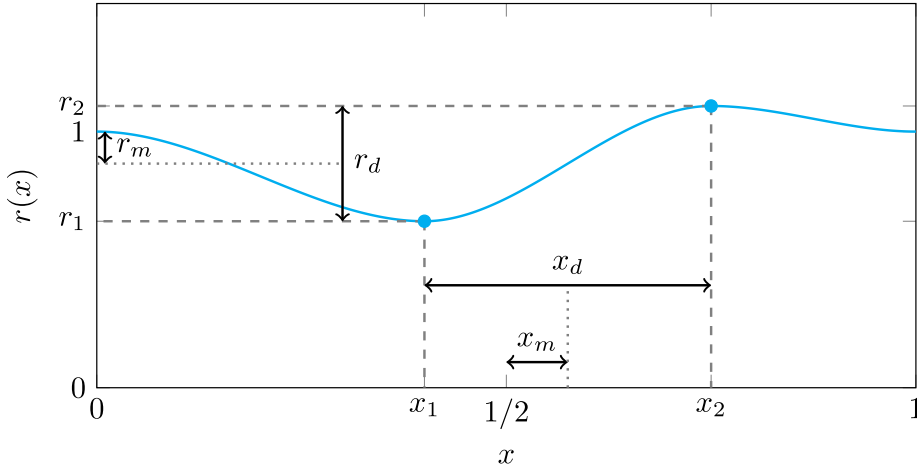


Fig. 3. Schematic illustration of the unit cell radius function $r(x)$. See Table 1 for the control parameters definition.

Let us close this section with a remark on the conditions under which only the quasi-plane waves propagate through the waveguide. The (dimensional) cut-off frequency f_c for an axially symmetrical waveguide with the maximum radius R_{\max} is given as:

$$f_c = \frac{1.83c_0}{2\pi R_{\max}}. \quad (12)$$

However, it shall be noted that this is a rather crude approximation based on an uniform waveguide (see e.g., [28] for full derivation by perturbation methods). In practice, it is necessary to design the systems so that the maximum frequency of interest is significantly below f_c .

It is useful to recall that an estimation of a characteristic frequency of the first band gap, the Bragg frequency f_B , is given as

$$f_B = \frac{c_0}{2\ell}, \quad (13)$$

where, again, ℓ is the (dimensional) length of the spatial period. From here, we can construct a rough estimate of the aspect ratio the unit cell must have for the first band gap to still be in the quasi-plane wave region. Obviously, one needs $f_B < f_c$ to hold and consequently

$$R_{\max} < 0.58\ell \quad (14)$$

or in lay language it can be roughly stated that the diameter of the tube must be noticeably smaller than the spatial period.

2.3. Parametrization of the waveguide geometry

The requirements for the parametrization of the waveguide geometry stem from the governing equations of transmission in locally periodic structures. Due to combined prerequisites of the Webster equation validity and the Floquet–Bloch theory, a smooth, slowly varying radius function $r(x)$ is needed and the unit cells have to be connected periodically and continuously to form a waveguide (i.e., $r(x=0) = r(x=1)$, see Section 2). There are no analytical solutions to this kind of profiles that can be expressed in terms of basic functions (for nontrivial variants see e.g., [29,30]) and hence there is no reason to prefer any specific type of radius function (e.g., sine square or fourth degree polynomial). For further data-driven discovery, it is essential that the impact of control parameters on the radius function $r(x)$ is clear and easy to interpret. While meeting the requirements, the particular choice of the unit cell radius function $r(x)$ can be arbitrary. To allow enough variability in the design of waveguide geometry, a cubic spline with four control parameters x_1, x_2, r_1, r_2 was chosen. In addition, it holds that $r(0) = r(1) = 1$ and the profile has zero slope at the beginning and at the end of the unit cell. For a schematic illustration, see Fig. 3 and for details on the cubic spline, see Appendix.

Since the behavior of the infinite periodic structure in this case is independent of the mirror symmetry of the unit cell, the description of the whole system should also be independent of swapping $x_1 \leftrightarrow x_2$ simultaneously with $r_1 \leftrightarrow r_2$. Hence, it is natural to introduce coordinate transformation that would promote this symmetry. The definitions and schematic depiction of the new control parameters x_m, x_d, r_m, r_d is given in Table 1 and Fig. 3.

3. Data processing and symbolic regression

Given the radius function $r(x)$, the Webster equation (3) for a unit cell and the conditions (5) is solved numerically using Runge–Kutta–Fehlberg method (RK45) with the initial conditions given by Eq. (5). The cosine of Bloch phase $\cos \xi$ is then obtained via

Table 1

Summary of the control parameters for the unit cell geometry. Note that not all their combinations are allowed due to the requirements of Webster equation. We limit the non-dimensional slope of the sections connecting the control points and the unit cell endpoints to be lower than 2 (e.g., $|r_1 - r_2|/|x_1 - x_2| < 2$).

Par.	Range	Formula	Interpretation
x_1	$\left[\frac{1}{4}, \frac{9}{20}\right]$	–	x coord. of the 1st control point
x_2	$\left[\frac{11}{20}, \frac{3}{4}\right]$	–	x coord. of the 2nd control point
r_1	$\left[\frac{1}{3}, 2\right]$	$r_1 = r(x_1)$	r coord. of the 1st control point
r_2	$\left[\frac{1}{3}, 2\right]$	$r_2 = r(x_2)$	r coord. of the 2nd control point
x_m	$\left[0, \frac{1}{3}\right]$	$x_m = \frac{1}{2}(x_1 + x_2) - \frac{1}{2}$	Excentricity of the avg. contr. point position
x_d	$\left[\frac{1}{5}, \frac{1}{2}\right]$	$x_d = x_1 - x_2 $	Distance between the control points on x
r_m	$\left[-\frac{1}{3}, \frac{2}{3}\right]$	$r_m = \frac{1}{2}(r_1 + r_2) - 1$	avg. deviation from the waveguide inlet width
r_d	$\left[0, \frac{3}{4}\right]$	$r_d = r_1 - r_2 $	Distance between the control points on r

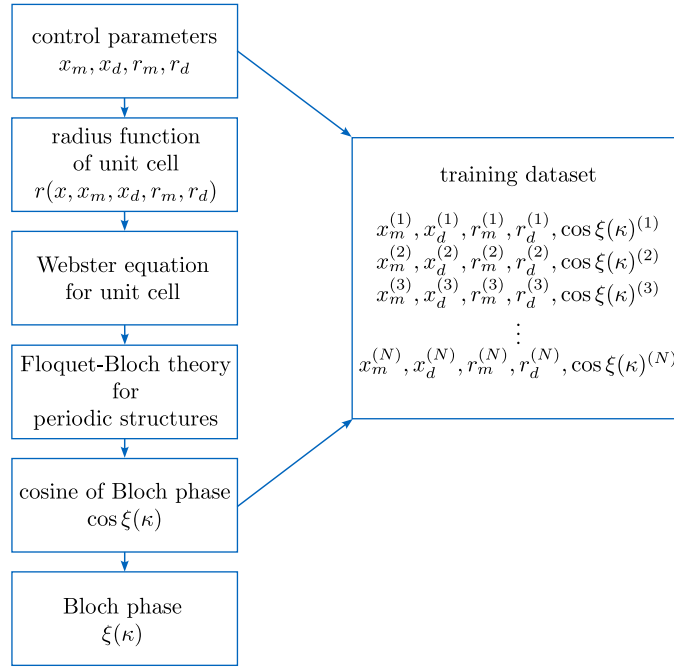


Fig. 4. Process of obtaining a dispersion relation for given waveguide geometry with schema, how the training dataset is prepared (where N is the total number of samples).

the Floquet–Bloch theory as explained in Section 2.2. In order to get the Bloch wave number μ and to plot the dispersion relation, arccosine of $\cos \xi$ divided by the non-dimensional period d is taken. For convenience, the process is illustrated in Fig. 4.

We aim to learn formulae modeling the acoustic transmission from the data generated by this numerical method. Since the last step of obtaining dispersion relation numerically is already known, there is no reason in trying to discover an already known relation (i.e. to let the algorithm learn the arc cosine). Instead, the dataset is built from the cosines of Bloch phases and related control parameters x_m, x_d, r_m and r_d . Further transformations of the dataset are described in relevant sections, Sections 4.1 and 4.3.

The useful physical information could be extracted from the dataset via basic regression methods given an appropriate library of terms. However, there is little to no insight into the exact relationship between control parameters x_m, x_d, r_m, r_d and the transmission. This aspect poses a problem: if we built our own library of candidate solutions it is likely that some intuition bias gets incorporated. For this reason, it is clear that the process of extracting formulae from data would benefit from a method, that would need as little guidance in the learning process as possible. The task is to find a model fitting the data with analytical relations as accurately as possible while being sparse and interpretable. This is a central problem of various symbolic regression techniques [22–24]. Here, we employ an open-source library PySR [31]. This tool builds expression trees from analytical terms and operators. Using a multi-population evolutionary algorithm, it searches over the space of possible expression trees for interpretable symbolic model.

A key aspect of the library setup is the choice of suitable candidate functions from which the expressions are constructed. In our experience, it is appropriate to address this problem for centers/widths of the bandgaps and the full dispersion relation separately.

The main difference is in the physical requirements for the candidate functions. For formulas for centers and widths, it does not matter too much if they are constructed from functions that locally do not have derivatives (as long as they are continuous). On the other hand, we need the dispersion relation to be differentiable at least by κ (e.g., for purposes of the group velocity estimation).

After a good deal of numerical experiments, the best choice in terms of simplicity, interpretability and accuracy was to assemble the formulae for centers and widths from functions \min , \max and binary operators $+$, $-$, $*$ and $/$ (see Section 4.1). To limit the over-importance of outliers, we employed L1-loss function.

For the case of the whole dispersion relation, we allow the functions \sin , \cos , \exp and the same basic binary operators (see Section 4.3). Here, the quantile loss function proved to be the best choice.

4. Discovered equations and their applications

This section will be dedicated to the results of the aforementioned symbolic regression. It will open with formulae for bandgap centers and widths (Section 4.1) followed by examples of their specific applications (Section 4.2). Subsequently, the focus will turn to the symbolic regression of the complete dispersion relation (Section 4.3).

Since it is somewhat tautological to compare the symbolic regression with the numerical solution of the Webster equation that served as its training, and because we would like to show the more practical aspects of our results, we test the results against a finite element simulation in Comsol Multiphysics. We use the simulation of the Helmholtz equation for the acoustic pressure in a 2D axially symmetric geometry. Unless otherwise stated (which happens only in Section 4.2.1), the domain consists of 30 unit cells. Their aspect ratio is chosen to allow the first three bandgaps to exist securely well below the cut-off frequency. A plane wave is prescribed at the input to the system using a background pressure field and its reflections at both ends of the domain are handled by perfectly matched layers. The transmission coefficient T is calculated using the magnitude of the complex sound pressure amplitude beyond the locally periodic structure.

In this section, the fluid (air) is considered inviscid and thermally non-conducting. The walls are perfectly rigid, with homogeneous Neumann condition for the acoustic pressure. In the discussion below (Section 5) it is shown that this aspect does not significantly change the validity of the formulas found.

4.1. Formulae for width and center of bandgaps

Before obtaining formulae for width and center of bandgaps via symbolic regression, their values (i.e. the ground truths in the sense of machine learning) are extracted from the dataset. The width of bandgaps are retrieved from the $\cos \xi$ as the width of range where $\cos \xi \leq 1$ for the first and the third gap and $\cos \xi \geq 1$ for the second gap. The centers lie in the middle of that range.

Let us begin with the formulae for the bandgap centers, denoted with m_1 , m_2 and m_3 for the first, second and third bandgap center, respectively. Recall, that we are using the nondimensional wavenumber κ , so the first, second and third Bragg frequency is π , 2π and 3π , respectively. Hence, it is natural to describe only the deviations from these values:

$$m_1 = \pi + 0.38 \max(0.17, x_d r_d) \quad (15)$$

$$m_2 = 2\pi + 0.3 [\max(r_m, r_d) - \min(0, r_d)] \quad (16)$$

$$m_3 = 3\pi + \max(0.25, r_d - r_m) \max(0.3, r_d) \quad (17)$$

Eqs. (15)–(17) are symbolic regression fits to bandgap centers ground truths. The summary statistics of errors is given in Fig. 5. It shows that Eqs. (15)–(17) describe the center frequencies very accurately. However, it is evident that this success has been achieved in no small part because the centers being described does not change much. This means that just a simple estimate using the Bragg frequency is reasonably accurate on its own. Note that this is very likely a feature of smooth geometries described by lossless Webster equation. It is not a general property of locally periodic structures.

Next, we move to the formulae for the widths of the first three gaps denoted with w_1 , w_2 and w_3 , respectively. As it happens in this kind of cases, we are forced to trade simplicity and interpretability of the formula for its accuracy in relatively small but troublesome parts of the dataset. Hence, we are showing two sets of formulae for the gap widths found via symbolic regression. First, the ones with lower complexity (denoted with a hat):

$$\hat{w}_1 = 2.61 [\max(r_m, r_d) - \min(0, r_m)] \quad (18)$$

$$\hat{w}_2 = 0.13 + \max[1.88(r_d - r_m), 4.67x_d r_m] \quad (19)$$

$$\hat{w}_3 = 0.53 r_d - 0.84 \min(0, r_m) \quad (20)$$

From here we can see several interesting functional (in)dependencies. The width of the first gap in Eq. (18) does not depend on the x -position of the control points, only on the relative addition or removal of the waveguide breadth. This implies that the decisive factor for the first gap is the change of unit cell overall volume (see the reasoning at the end of Appendix). In addition, it is clear that decreasing the cross-sectional area has a relatively greater effect on the 1st gap width than increasing it. To explain this phenomenon, just recall the remarks on Gaussian curvature above. The latter trait are present even in Eqs. (19)–(20) as well (both contain terms dependent on negative r_m).

Although Eqs. (19)–(20) are well-suited for reading overall tendencies, they evidently suffer from physical inconsistencies. For instance, according to Eq. (19) even a straight tube would have a small 2nd gap. Moreover, even the summary statistics of errors is not in favor of \hat{w}_2 , \hat{w}_3 (see Fig. 6). Hence, it is necessary to come up with more elaborate relations:

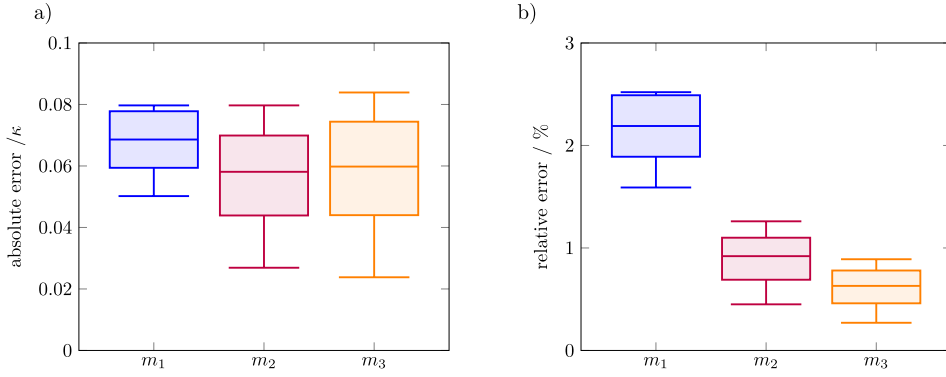


Fig. 5. Error on testing dataset for bandgap center prediction (Eqs. (15)–(17)). The box is indicating the median and the interquartile range, the whiskers 8th and 92th percentile of error. (a) the absolute error measured in κ , (b) the relative error.

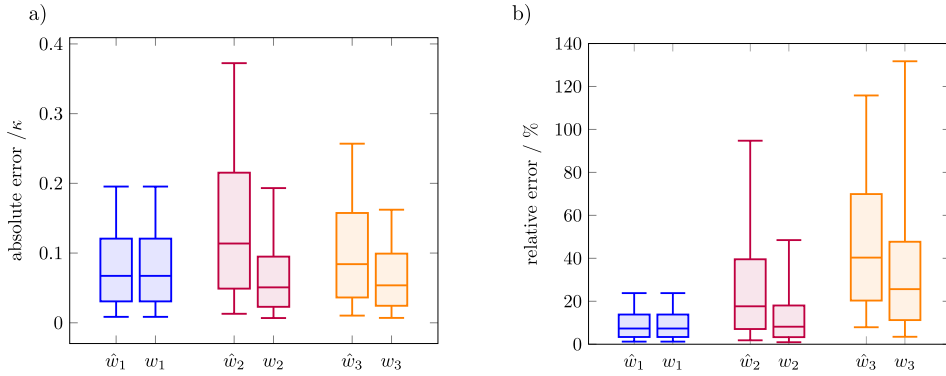


Fig. 6. Error on testing dataset for bandgap width prediction (Eqs. (21)–(23)). The box is indicating the median and the interquartile range, the whiskers 8th and 92th percentile of error. Note that the hat is indicating the results of relations with lower complexity (Eqs. (18)–(20)). (a) the absolute error measured in κ , (b) the relative error.

$$w_1 = 2.61 [\max(r_m, r_d) - \min(0, r_m)] \quad (21)$$

$$w_2 = \max(4.95x_d r_m, r_d) - (r_d + 0.11) [(1.85x_d - 1.01) + 5.62 \min(r_m - x_m, x_m)] \quad (22)$$

$$w_3 = \max[\min(x_d, r_m), (r_d - r_m)] \frac{\max(x_d, 0.7 - x_d)}{0.37 - x_m} - 0.46 \quad (23)$$

Eqs. (18) and (21) are identical because the simpler relationship was applicable to the same degree of accuracy as the more complex ones (see Fig. 6). The more elaborated equations (21)–(23) are a bit harder to read but still very simple to be implemented in an auxiliary script for evaluation and simple optimization or useful special cases can be derived from them. We will show both in the following section.

4.2. Specific examples of application

4.2.1. Targeted bandgap with simple geometry constraints

To illustrate the use of our formulae, we first give a simple example of the application of Eqs. (15) and (21) to a made-up practice-motivated problem. Suppose we have about 8.5 m of circular ventilation pipe with a diameter of 300 mm. The task is to block a 50 Hz wide frequency band centered at 210 Hz (this might correspond to the blade passage frequency of a fan, for example). Further assume that for construction reasons nothing can be added to the pipe diameter. On the contrary, we consider only inserts within the tube. Finally, suppose that a relatively cooler air is inside the pipe so that $c_0 = 335 \text{ m s}^{-1}$.

First, we use Eq. (15) to assess the non-dimensional wavenumber of the first gap center frequency as $\kappa_c = 3.2$ (i.e. slightly above π). Next, the (dimensional) wavenumber corresponding to $\bar{f} = 210 \text{ Hz}$ is $2\pi\bar{f}/c_0 = 3.94 \text{ m}^{-1}$. Since $\kappa_1 = 2\pi\bar{f}\ell/c_0$, we can determine the unit cell length $\ell = 0.81 \text{ m}$. Thus, on a given length of 8.5 m we can have a locally periodic structure with 10 unit cells. By analogous calculation, we find that the dimensionless width w_1 corresponding to the 50 Hz band should have a value of 0.94. This figure can be used in Eq. (21) to design the specific geometry.

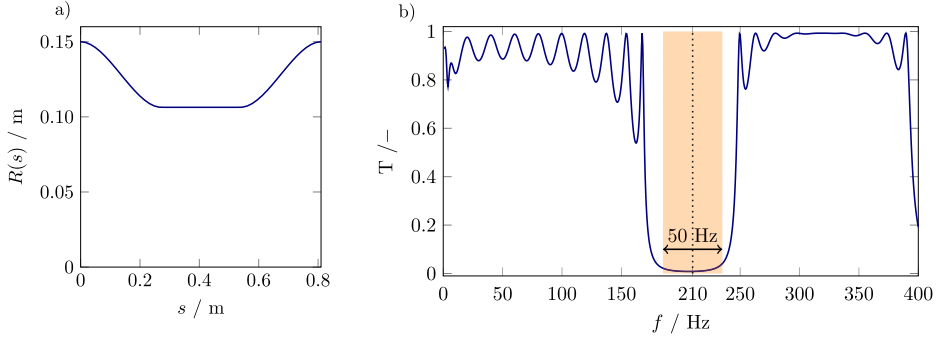


Fig. 7. Results for application example on targeted bandgap with simple geometry constraints: (a) the radius function of the unit cell; (b) its transmission characteristic with the intended bandgap and its center marked.

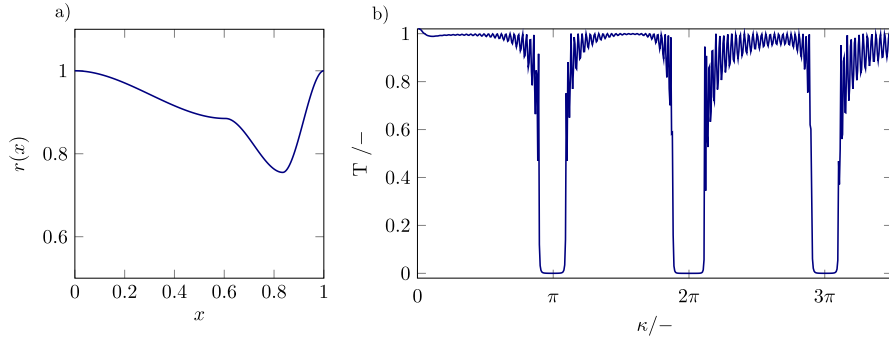


Fig. 8. Results for application example on three equally wide bandgaps: (a) radius function of the unit cell; (b) the corresponding transmission characteristic.

There are an infinite number of ways to meet this requirement, but there are some limiting conditions. Recall that we are only considering inserts inside the pipe and if it were to be a very low mach number flow ventilation pipe, for instance, we would require a smooth profile for hydrodynamic reasons. Hence, the following choice is natural:

$$x_m = 0, \quad x_d = 0.33, \quad r_m = -0.29, \quad r_d = 0. \quad (24)$$

Finally, it remains to transform these relations back into (dimensional) geometric quantities. The results are given in Fig. 7. Evidently, the bandwidth and its center are correctly sized, and the transmission coefficient is low enough to call the whole design successful even with only ten unit cells.

In the general case, however, a problem may arise in a locally periodic structure that is not covered by Eqs. (21)–(23). The bandgap widths are derived for the case of an infinite periodic structure and thus do not consider the possibility that an evanescent wave might be able to propagate far enough through the local structure. This would result in a higher than zero transmission coefficient. To this end, it makes sense to have formulae for the complete dispersion relation as well (see Section 4.3 below).

4.2.2. Three equally wide bandgaps

For the type of locally periodic structures studied, it is quite common that the width of the first bandgap is larger than the width of the second one and the same goes for the third one. To show the capabilities of the analytical formulae (21)–(23), we find a case with three bandgaps of approximately same width. To that end we minimize the value of

$$(w_1 - w_2)^2 + (w_1 - w_3)^2 + (w_2 - w_3)^2 + \max(0.5 - w_1, 0) \quad (25)$$

by means of simple coordinate descent optimization algorithm. The resulting radius function and the transmission characteristic are given in Fig. 8.

4.2.3. Constant second bandgap with different geometries

Although the full form of Eqs. (21)–(23) is relatively complicated, it can be used to derive some tractable special cases. Let us show that on a specific example. We assume $x_m = 0$, $r_d = 0$ and $r_m > 0$, i.e. the unit cell consists of a protrusion with a flat tip. For these assumptions we obtain the total differential of Eq. (22) in the following form:

$$dw_2 = (4.95r_m - 0.2) dx_d + 4.95x_d dr_m. \quad (26)$$

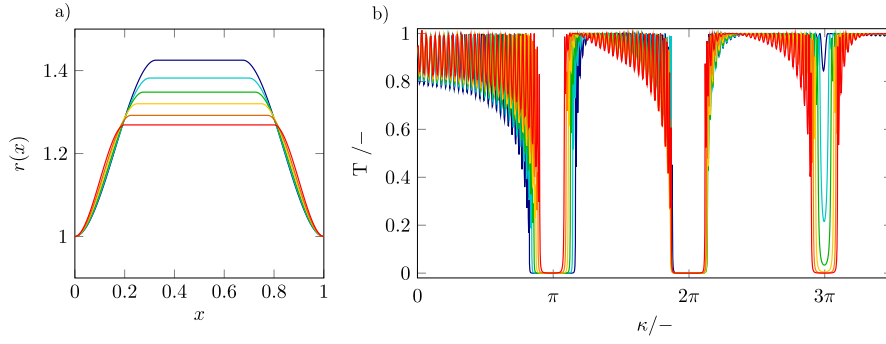


Fig. 9. Results for application example on constant second bandgap with different geometries: (a) different unit cell geometries designed to satisfy $dw_2 = 0$ in Eq. (26). (b) The corresponding transmission characteristics. (For interpretation of the references to color in this figure legend, the reader is referred to the web version of this article.)

One possible use of this equation is as a guide to changing r_m and x_d so that w_2 remains the same. This effect demonstrated in Fig. 9. Parameters of the second bandgap are constant while the first and third ones are varying. Note that the physical interpretation of the formula for the first bandgap width (Eq. (18)) is again confirmed, because w_1 is clearly dependent on the volume of the unit cell. The converse case can also be supported by the interpretation that the third bandgap (i.e., relatively shorter wavelengths) is better supported by more localized changes in the radius function. Roughly speaking, the reddish radius curves in Fig. 9 contain a relatively larger fraction of the constant portion of the waveguide and then steeper changes at the beginning and end of the unit cell.

4.3. Formulae for dispersion relation prediction

To extract formulae for prediction of cosine of Bloch phase $\cos \xi(\kappa, x_m, x_d, r_m, r_d)$ from the dataset, the first step is to find a coordinate transform into lower-dimensional space that simplifies the system. By applying principal component analysis (PCA) on the dataset of cosines of Bloch phase $\cos \xi$, we find new bases vectors $b_i(\kappa)$, dependent only on the dimensionless wavenumber, and new coordinates $c_i(x_m, x_d, r_m, r_d)$, dependent only on the radius function features. This means we can express the original $\cos \xi$ as $\cos \xi = b_0 + \sum_{i=1}^n b_i c_i$, where b_0, n is the mean of all cosines of Bloch phases $\cos \xi$ and the dimension of the new coordinate system, respectively.

It follows that the bases b_i are arrays of values shared by the entire dataset and the coordinates c_1, c_2, c_3 are scalars characteristic for each specific unit cell geometry. Our goal is to fit the bases b_i with a function of a single variable κ and to find a relationship between the coordinates c_i and the control parameters, x_m, x_d, r_m and r_d .

For this dataset, the bases b_1, b_2, b_3 (depicted in Fig. 10) preserve 99.99% of the original information (the explained variance) in the model (92.25%, 7.35% and 0.39%, respectively). Hence, we can express the cosine of the Bloch phase as

$$\cos \xi = b_0 + b_1 c_1 + b_2 c_2 + b_3 c_3, \quad (27)$$

where the formulae for bases functions $b_i(\kappa)$ were fitted with the use of symbolic regression as:

$$b_0(\kappa) = 1.054 \cos(\kappa) - 0.115 \sin(0.587\kappa) - 0.026, \quad (28)$$

$$b_1(\kappa) = 1.134 \cos(0.883\kappa) + 0.193\kappa - 1.279 - 5.8 \cdot 10^{-6} \exp(\kappa), \quad (29)$$

$$b_2(\kappa) = -0.037\kappa \cos(0.617\kappa) + 0.032\kappa - 1.6 \cdot 10^{-6} \exp(\kappa), \quad (30)$$

$$b_3(\kappa) = 0.009 \kappa [\sin(0.857\kappa) - \sin(-0.105\kappa)], \quad (31)$$

and for the coordinates $c_i(x_m, x_d, r_m, r_d)$ the fitted equations read:

$$c_1 = -0.134 \cos(2.990r_m) + \frac{r_d^2 + 0.073}{3.894r_m + 2.448 - r_d}, \quad (32)$$

$$c_2 = -(9.196x_m + 0.305) \frac{r_m r_d}{r_m + 0.529}, \quad (33)$$

$$c_3 = 0.033 - 0.710x_m \left(\frac{x_m}{x_d^2} + 2r_d \right) \left(r_m + \frac{r_d}{r_m + 0.390} \right). \quad (34)$$

Two illustrative examples from the training dataset, where the numerical solution of the Webster equation used for training are compared to the extracted formulae, can be seen in Figs. 11 and 12. In the first case, the difference between the numerical solution and the prediction is barely noticeable. The latter illustrates that not all predictions fit that well and that the transmission model

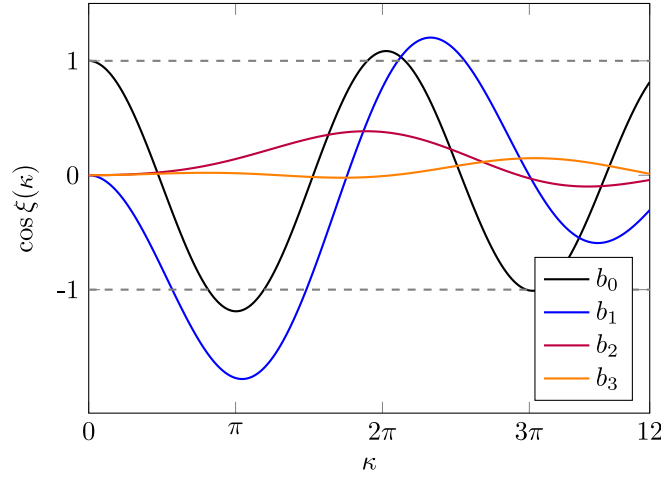


Fig. 10. PCA results, mean cosine of Bloch phase b_0 and the new bases vectors b_1, b_2, b_3 shared by the entire training dataset.

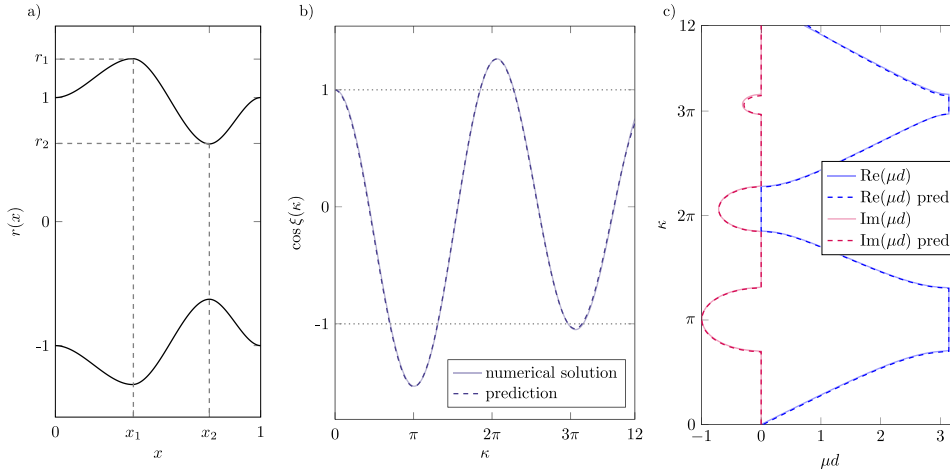


Fig. 11. Example from the training dataset: (a) Unit cell radius function $r(x)$; (b) comparison of the numerical solution and prediction in terms of cosine of Bloch phase $\cos \xi$; (c) comparison of the numerical solution and prediction transformed to dispersion relation.

is very sensitive to misfitting around $\cos \xi = -1$ and $\cos \xi = 1$: because of the arccosine properties, a slight misfit can have crucial impact on predicting whether the bandgap should be opened or not.

In Fig. 13, the error on testing dataset is depicted. A minor error has been introduced into the system already at the beginning with the coordinate transform. Since fitting both b_i and c_i is a trade-off between accuracy of prediction and simplicity of the extracted formulae, it is impossible to reduce the error on the training dataset while still keeping interpretability of the model.

As in the previous section, we can show that the discovered equations do not lack a physical interpretation. It is easy to prove that for a radius function $r(x) = \text{const.}$ holds that $\cos \xi = \cos \kappa$. In this sense, the base b_0 (Eq. (28)) differs from the uniform waveguide only by a very small correction. This interpretation is natural because it follows that b_0 is a typical “mean value” or the “zeroth term of the series”.

Next, note from Fig. 10 that b_1 is essentially the only one active in the region around $\kappa \approx \pi$, i.e. in the region of the first bandgap. This corresponds to the fact that the equation for c_1 (Eq. (32)) contains a dependence on the same parameters as the equation for the width of the first gap w_1 (Eq. (21)), i.e. that it is independent of x_m and x_d . Moreover, r_m is the most influential variable. Among other possibilities, let us choose, for example, that to control the second gap independently of the first one (i.e. to control b_2 and c_2), we need both parameters r_d and r_m active, preferably with x_m offset as well (see Eq. (33)). This is in correspondence with the fact that many simple radius functions have the properties of the first and second gaps relatively tightly coupled.

5. Discussion

Before proceeding to more extensive topics, just two short remarks. The accuracy of the equations found on the training dataset was always compared against the test dataset to rule out the possibility of overfitting. However, the accuracy remained the same

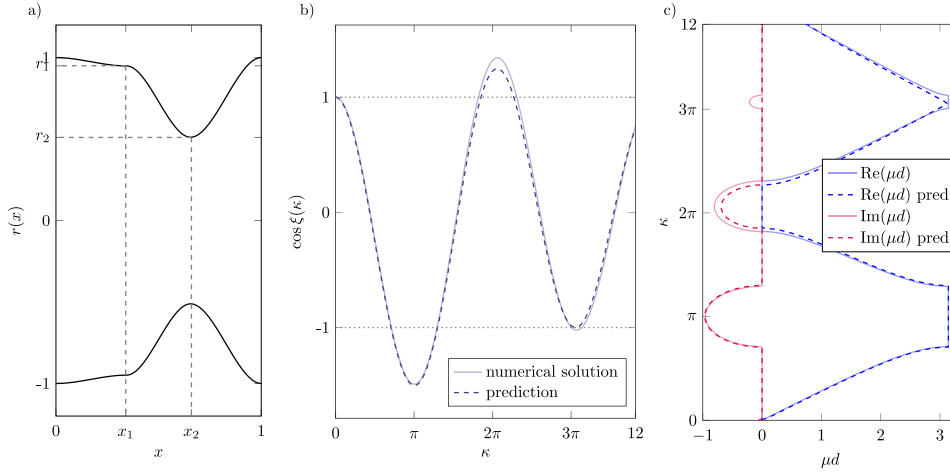


Fig. 12. Example from the training dataset: (a) Unit cell radius function $r(x)$; (b) comparison of the numerical solution and prediction in terms of cosine of Bloch phase $\cos \xi$; (c) comparison of the numerical solution and prediction transformed to dispersion relation.

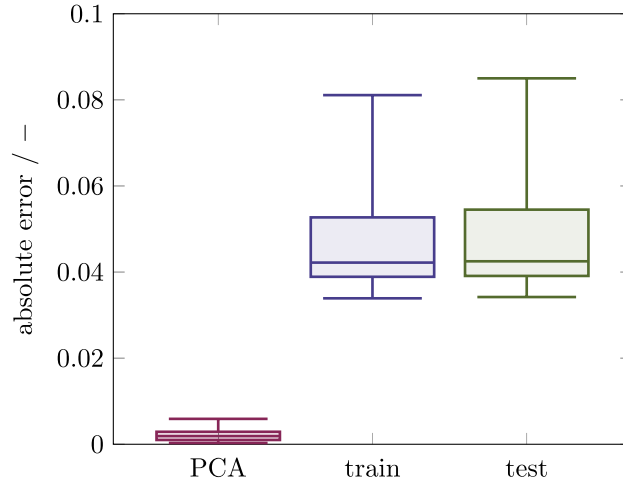


Fig. 13. Error on training and testing dataset. The error was obtained as the maximum difference between numerical solution and prediction in terms of cosine of Bloch phase $\cos \xi$.

for both the training and the validation dataset for expressions roughly twice as large as the longest one listed in the results section. For these reasons, we did not need to address the overfitting phenomenon.

In the early stages of our work on this paper, we tried to use radius functions with a more straightforward analytical formulation (e.g., sine squared). However, the benefit of greater ease of writing did not outweigh the significantly reduced ability to control bandgap parameters. We consider the cubic splines with two control points employed here to be a good compromise between variability and presentability.

5.1. Applications of the results on related problems

We first discuss the application of the results of the previous sections to related wave phenomena. Before addressing other types of wave equations in inhomogeneous media, let us recall that a more general results are immediately obtained from the properties of the cross-section geometry alone. The exact same modification that leads from the cross-section function $A(x)$ to the radius function $R(x)$

$$\frac{1}{A(x)} \frac{dA(x)}{dx} \rightarrow \frac{2}{R(x)} \frac{dR(x)}{dx} \quad (35)$$

holds for any cross-sectional shape that can be described by a single linear parameter (such as the side of a square, the side of a rectangle with a fixed aspect ratio or an ellipse of constant eccentricity to name a few).

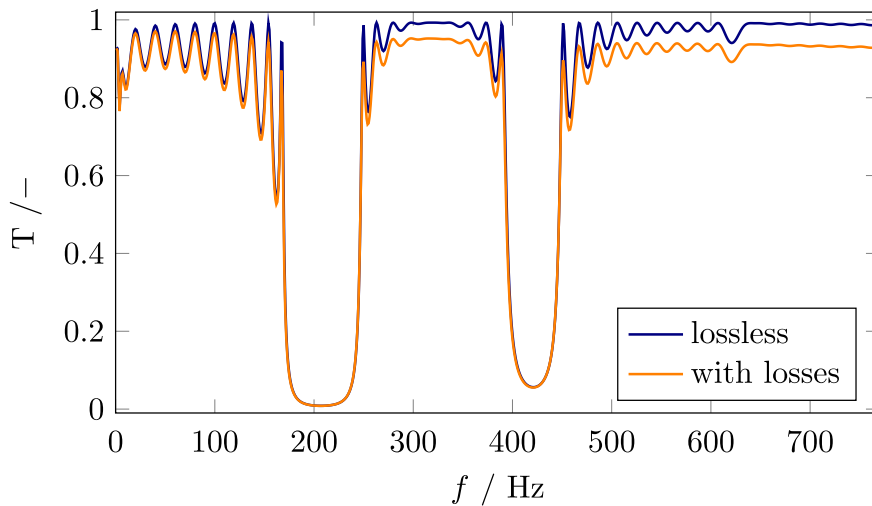


Fig. 14. Comparison of lossless and lossy transmission characteristics on a geometry from the example of Section 4.2.1.

In a simple case of quasi one-dimensional flow in which the effects on the sound field are dominated by convection (i.e., low Mach number, no significant vortex shedding etc.) it is possible to generalize the Webster horn equation (2) to the nozzle equation of the form [32,33]:

$$\frac{d^2\phi}{dx^2} + \left(\frac{2}{R} \frac{dR}{dx} + 2i \frac{\omega}{c_0} M \right) \frac{d\phi}{dx} + \frac{\omega^2}{c_0^2} \phi = 0 \quad (36)$$

where $M = M(x)$ stands for the (local, spatially dependent) Mach number and ϕ is the acoustic velocity potential. The latter equation is formally different from Eq. (2) due to the second term in the bracket. However, our numerical experiments with linearized Euler equations clearly show that the influence of the convection (even with reasonably curved walls not allowing for strong production of vorticity) are insignificant in this case (typical Mach numbers $M < 0.05$). Hence, we assume the formulae given in Sections 4.1 and 4.3 to be applicable in scenarios with low Mach number flow in wide ducts (e.g. in ventilation systems) at least as a handy approximation. This paves the way for the application of this paper in the field of ventilated metamaterials (see e.g., [4]).

In a slender rod with varying cross-section formally the same wave equation as Eq. (2) governs the displacement field due to longitudinal elastic waves (see e.g., [29]). In this case, the above results are equally valid.

5.2. Effect of neglecting the thermoviscous losses

As mentioned in the Introduction, we study the selected system as non-dissipative. Here we briefly show how this approximation, which is strictly speaking non-physical, affects the results. Let us return to the example described in Section 4.2.1. We now perform the simulation once more and in a wider frequency range and both for the lossless and the lossy case. The thermoviscous losses here are captured employing an effective medium with changing characteristic hydraulic diameter (implemented in Comsol as Narrow Region Acoustics – Wide duct approximation).

The results are given in Fig. 14. Although the transmission characteristic curve is somewhat skewed towards high frequencies in the case with losses, the quantitative differences are not large and the qualitative ones (e.g. the width of the gaps or the importance of the occurrence of the third gap) are essentially absent altogether. The physical justification is straightforward: given the frequency range and the geometrical proportions, the acoustic boundary layer occupies only a very small part of the cross-section. This will be the situation in the vast majority of cases covered in this article.

6. Conclusions

We studied one-dimensional sonic crystals governed by the Webster equation. For the sake of generality, the geometry was described as a cubic spline with two control points, which provided enough flexibility to investigate and control the first three bandgaps. Based on the application of Floquet–Bloch theory and advanced symbolic regression, formulae for the centers and widths of the bandgaps as well as for the entire dispersion relation were found. In many cases, the relationships obtained by machine learning were also supported by physical interpretation. Although the object of study was an axially symmetric waveguide filled with ideal gas and supporting quasi-plane waves, it was shown that the results are not limited to this particular geometry. Moreover, the formulae found are valid with equal accuracy for longitudinal waves in a slender rod of variable cross-section and furthermore as a good approximation also for non-uniform ducts with flow at very low Mach numbers.

Furthermore, in addition to its contribution to the acoustics of locally periodic structures, this paper is a stepping stone for the study of analogous Sturm–Liouville type problems in various wave phenomena (see e.g., [17,34–37]) from the perspective of physics informed machine learning.

CRediT authorship contribution statement

Viktor Hruška: Writing – original draft, Methodology, Investigation, Formal analysis, Conceptualization. **Aneta Furmanová:** Writing – original draft, Software, Methodology, Investigation. **Michal Bednařík:** Writing – review & editing, Validation, Supervision, Project administration, Funding acquisition.

Declaration of competing interest

The authors declare the following financial interests/personal relationships which may be considered as potential competing interests: Michal Bednarik reports financial support was provided by Czech Science Foundation. If there are other authors, they declare that they have no known competing financial interests or personal relationships that could have appeared to influence the work reported in this paper.

Acknowledgments

This work was supported by the Czech Science Foundation (GACR) grant No. 22-33896S.

Appendix. Cubic splines

We assume x_1 , x_2 , r_1 and r_2 to be given and the unit cell spanning from $x = 0$ to $x = 1$. Then we can write the portions of the radius function as $r(x) = a_3x^3 + a_2x^2 + a_1x + a_0$ with the constants a_i given as follows:

- For $0 \leq x < x_1$:

$$a_0 = 1 \quad (\text{A.1})$$

$$a_1 = 0 \quad (\text{A.2})$$

$$a_2 = \frac{3(r_1 - 1)}{x_1^2} \quad (\text{A.3})$$

$$a_3 = -\frac{2(r_1 - 1)}{x_1^3} \quad (\text{A.4})$$

- For $x_1 \leq x \leq x_2$:

$$a_0 = \frac{3r_1x_1x_2^2 - r_1x_2^3 + r_2x_1^3 - 3r_2x_1^2x_2}{(x_1 - x_2)^3} \quad (\text{A.5})$$

$$a_1 = -\frac{6x_1x_2(r_1 - r_2)}{(x_1 - x_2)^3} \quad (\text{A.6})$$

$$a_2 = \frac{3(r_1 - r_2)(x_1 + x_2)}{(x_1 - x_2)^3} \quad (\text{A.7})$$

$$a_3 = \frac{2(r_2 - r_1)}{(x_1 - x_2)^3} \quad (\text{A.8})$$

- For $x_2 < x \leq 1$:

$$a_0 = \frac{x_2^3 + 3r_2x_2 - 3x_2^2 - r_2}{(x_2 - 1)^3} \quad (\text{A.9})$$

$$a_1 = -\frac{6x_2(r_2 - 1)}{(x_2 - 1)^3} \quad (\text{A.10})$$

$$a_2 = \frac{3(r_2 - 1)(x_2 + 1)}{(x_2 - 1)^3} \quad (\text{A.11})$$

$$a_3 = \frac{2(1 - r_2)}{(x_2 - 1)^3} \quad (\text{A.12})$$

Based on these equations, it is possible to calculate the volume of a unit cell V . The resulting formula is rather tedious, but a valuable expression can be obtained from taking the multiple Taylor expansion around $x_1 = 1/4$, $x_2 = 3/4$, $r_1 = r_2 = 1$ (i.e. around the uniform tube parameters). Neglecting the second order terms one obtains:

$$\frac{V}{\pi} \approx -\frac{1}{2} + \frac{3}{4}(r_1 + r_2) \equiv 1 + \frac{3}{2}r_m \quad (\text{A.13})$$

It follows that the dependence on x_1 , x_2 is at least a second order correction. The same applies to the control point difference measured on r (variable r_d).

Data availability

Data will be made available on request.

References

- [1] A. Gupta, A review on sonic crystal, its applications and numerical analysis techniques, *Acoust. Phys.* 60 (2) (2014) 223–234, <http://dx.doi.org/10.1134/s1063771014020080>.
- [2] N. Jiménez, O. Umnova, J.-P. Groby, *Acoustic Waves in Periodic Structures, Metamaterials, and Porous Media: From Fundamentals to Industrial Applications*, Springer International Publishing, 2021, <http://dx.doi.org/10.1007/978-3-030-84300-7>.
- [3] V. Romero-Garcia, A. Hladky-Hennion, *Fundamentals and Applications of Acoustic Metamaterials: From Seismic to Radio Frequency*, Wiley, 2019.
- [4] J. Zhang, B. Hu, S. Wang, Review and perspective on acoustic metamaterials: From fundamentals to applications, *Appl. Phys. Lett.* 123 (1) (2023) <http://dx.doi.org/10.1063/5.0152099>.
- [5] Muhammad, C.W. Lim, From photonic crystals to seismic metamaterials: A review via phononic crystals and acoustic metamaterials, *Arch. Comput. Methods Eng.* 29 (2) (2021) 1137–1198, <http://dx.doi.org/10.1007/s11831-021-09612-8>.
- [6] Muhammad, J. Kennedy, C. Lim, Machine learning and deep learning in phononic crystals and metamaterials – A review, *Mater. Today Commun.* 33 (2022) 104606, <http://dx.doi.org/10.1016/j.mtcomm.2022.104606>.
- [7] B. Zheng, J. Yang, B. Liang, J.-c. Cheng, Inverse design of acoustic metamaterials based on machine learning using a Gauss–Bayesian model, *J. Appl. Phys.* 128 (13) (2020) <http://dx.doi.org/10.1063/5.0012392>.
- [8] M. Sigalas, M.S. Kushwaha, E.N. Economou, M. Kafesaki, I.E. Psarobas, W. Steurer, Classical vibrational modes in phononic lattices: theory and experiment, *Z. Kristallographie - Cryst. Mater.* 220 (9–10) (2005) 765–809, <http://dx.doi.org/10.1524/zkri.2005.220.9-10.765>.
- [9] V. Laude, Phononic Crystals: Artificial Crystals for Sonic, Acoustic, and Elastic Waves, De Gruyter, 2020, <http://dx.doi.org/10.1515/9783110641189>.
- [10] P.D.C. King, T.J. Cox, Acoustic band gaps in periodically and quasiperiodically modulated waveguides, *J. Appl. Phys.* 102 (1) (2007) <http://dx.doi.org/10.1063/1.2749483>.
- [11] S. Sepehri, M.M. Mashhadi, M.M.S. Fakhrabadi, Wave propagation in nonlinear monoatomic chains with linear and quadratic damping, *Nonlinear Dynam.* 108 (1) (2022) 457–478, <http://dx.doi.org/10.1007/s11071-021-07184-7>.
- [12] S. Sepehri, M.M. Mashhadi, M.M.S. Fakhrabadi, Wave propagation in fractionally damped nonlinear phononic crystals, *Nonlinear Dynam.* 110 (2) (2022) 1683–1708, <http://dx.doi.org/10.1007/s11071-022-07704-z>.
- [13] B. Zhao, H.R. Thomsen, X. Pu, S. Fang, Z. Lai, B.V. Damme, A. Bergamini, E. Chatzi, A. Colombi, A nonlinear damped metamaterial: Wideband attenuation with nonlinear bandgap and modal dissipation, *Mech. Syst. Signal Process.* 208 (2024) 111079, <http://dx.doi.org/10.1016/j.ymssp.2023.111079>.
- [14] I. Nuskinsky, A.A. Hardy, Band-gap analysis of one-dimensional photonic crystals and conditions for gap closing, *Phys. Rev. B* 73 (12) (2006) <http://dx.doi.org/10.1103/physrevb.73.125104>.
- [15] G.V. Morozov, D.W.L. Sprung, Floquet–Bloch waves in one-dimensional photonic crystals, *Europhys. Lett.* 96 (5) (2011) 54005, <http://dx.doi.org/10.1209/0295-5075/96/54005>.
- [16] S. Caffrey, G.V. Morozov, D.W.L. Sprung, J. Martorell, Floquet–Bloch solutions in a sawtooth photonic crystal, *Opt. Quantum Electron.* 49 (3) (2017) <http://dx.doi.org/10.1007/s11082-017-0939-1>.
- [17] M. Bednarik, M. Cervenka, Propagation of electromagnetic waves through non-uniform dielectric layers, *J. Opt. Soc. Am. B* 35 (10) (2018) 2541, <http://dx.doi.org/10.1364/josab.35.002541>.
- [18] J. Deng, O. Guasch, D. Ghilardi, Solution and analysis of a continuum model of sonic black hole for duct terminations, *Appl. Math. Model.* 129 (2024) 191–206, <http://dx.doi.org/10.1016/j.apm.2024.01.046>.
- [19] J. Deng, O. Guasch, Sound waves in continuum models of periodic sonic black holes, *Mech. Syst. Signal Process.* 205 (2023) 110853, <http://dx.doi.org/10.1016/j.ymssp.2023.110853>.
- [20] S.L. Brunton, J.N. Kutz, *Data-Driven Science and Engineering: Machine Learning, Dynamical Systems, and Control*, second ed., Cambridge University Press, 2022.
- [21] G.E. Karniadakis, I.G. Kevrekidis, L. Lu, P. Perdikaris, S. Wang, L. Yang, Physics-informed machine learning, *Nat. Rev. Phys.* 3 (6) (2021) 422–440, <http://dx.doi.org/10.1038/s42254-021-00314-5>.
- [22] G. Camps-Valls, A. Gerhardus, U. Ninad, G. Varando, G. Martius, E. Balaguer-Ballester, R. Vinuesa, E. Diaz, L. Zanna, J. Runge, Discovering causal relations and equations from data, *Phys. Rep.* 1044 (2023) 1–68, <http://dx.doi.org/10.1016/j.physrep.2023.10.005>.
- [23] S.-M. Udrescu, M. Tegmark, AI feynman: A physics-inspired method for symbolic regression, *Sci. Adv.* 6 (16) (2020) eaay2631, <http://dx.doi.org/10.1126/sciadv.aay2631>.
- [24] M. Schmidt, H. Lipson, Distilling free-form natural laws from experimental data, *Science* 324 (5923) (2009) 81–85, <http://dx.doi.org/10.1126/science.1165893>.
- [25] A. Gupta, K.M. Lim, C.H. Chew, Analysis of frequency band structure in one-dimensional sonic crystal using Webster horn equation, *Appl. Phys. Lett.* 98 (20) (2011) <http://dx.doi.org/10.1063/1.3592570>.
- [26] D.T. Blackstock, *Fundamentals of Physical Acoustics*, Wiley, 2000, p. 422.
- [27] M.I. Hussein, M.J. Frazier, Band structure of phononic crystals with general damping, *J. Appl. Phys.* 108 (9) (2010) <http://dx.doi.org/10.1063/1.3498806>.
- [28] S.W. Rienstra, Webster’s Horn equation revisited, *SIAM J. Appl. Math.* 65 (6) (2005) 1981–2004, <http://dx.doi.org/10.1137/s0036139902413040>.
- [29] M. Bednarik, M. Cervenka, A wide class of analytical solutions of the Webster equation, *J. Sound Vib.* 469 (2020) 115169, <http://dx.doi.org/10.1016/j.jsv.2019.115169>.
- [30] V. Hruška, M. Reiser, M. Bednarik, Fast design of non-uniform acoustic waveguides with prescribed eigenfrequencies, *Wave Motion* 122 (2023) 103192, <http://dx.doi.org/10.1016/j.wavemoti.2023.103192>.
- [31] M. Cranmer, Interpretable machine learning for science with PySR and SymbolicRegression.jl, 2023, <http://dx.doi.org/10.48550/ARXIV.2305.01582>.
- [32] L. Campos, F. Lau, On the acoustics of low Mach number bulged, throated and baffled nozzles, *J. Sound Vib.* 196 (5) (1996) 611–633, <http://dx.doi.org/10.1006/jsvi.1996.0505>.
- [33] L. Campos, On 36 forms of the acoustic wave equation in potential flows and inhomogeneous media, *Appl. Mech. Rev.* 60 (2007) 149–171.
- [34] M. Bednarik, M. Cervenka, Electromagnetic waves in graded-index planar waveguides, *J. Opt. Soc. Am. B* 37 (12) (2020) 3631, <http://dx.doi.org/10.1364/josab.408679>.
- [35] M. Bednarik, M. Cervenka, J. Groby, P. Lotton, One-dimensional propagation of longitudinal elastic waves through functionally graded materials, *Int. J. Solids Struct.* 146 (2018) 43–54, <http://dx.doi.org/10.1016/j.ijsolstr.2018.03.017>.
- [36] M. Bednarik, M. Cervenka, P. Lotton, L. Simon, Analytical solutions for elastic SH-waves propagating through an isotropic inhomogeneous layer, *Compos. Struct.* 220 (2019) 875–887, <http://dx.doi.org/10.1016/j.compstruct.2019.04.053>.
- [37] M. Bednarik, M. Cervenka, P. Lotton, G. Penelet, Behavior of plane waves propagating through a temperature-inhomogeneous region, *J. Sound Vib.* 362 (2016) 292–304, <http://dx.doi.org/10.1016/j.jsv.2015.10.010>.